



# Two Orders of Magnitude Variation in the Star Formation Efficiency across the Premerger Galaxy NGC 2276

Neven Tomičić<sup>1</sup> , Annie Hughes<sup>2,3</sup> , Kathryn Kreckel<sup>1</sup> , Florent Renaud<sup>4</sup> , Jérôme Pety<sup>5</sup> , Eva Schinnerer<sup>1</sup> , Toshiki Saito<sup>1</sup> , Miguel Querejeta<sup>6,7</sup> , Christopher M. Faesi<sup>1</sup> , and Santiago Garcia-Burillo<sup>7,8</sup>

<sup>1</sup>Max Planck Institute for Astronomy (MPIA), Königstuhl 17, D-69117 Heidelberg, Germany; [tomicic@mpia-hd.mpg.de](mailto:tomicic@mpia-hd.mpg.de)

<sup>2</sup>Université de Toulouse, UPS-OMP, F-31028 Toulouse, France

<sup>3</sup>CNRS, IRAP, Av. du Colonel Roche BP 44346, F-31028 Toulouse cedex 4, France

<sup>4</sup>Department of Astronomy and Theoretical Physics, Lund Observatory, Box 43, SE-221 00 Lund, Sweden

<sup>5</sup>IRAM, 300 rue de la Piscine, F-38406 Saint Martin d'Hères, France

<sup>6</sup>European Southern Observatory, Karl-Schwarzschild Strasse 2, D-85748 Garching bei München, Germany

<sup>7</sup>Observatorio Astronómico Nacional (OAN), C/Alfonso XII 3, Madrid E-28014, Spain

<sup>8</sup>Observatorio Astronómico Nacional, Aptdo 1143, E-28800 Alcalá de Henares, Spain

Received 2018 September 19; revised 2018 December 11; accepted 2018 December 11; published 2018 December 21

## Abstract

We present the first spatially resolved ( $\sim 0.5$  kpc) measurements of the molecular gas depletion time  $\tau_{\text{depl}}$  across the disk of the interacting spiral galaxy NGC 2276, a system with an asymmetric morphology in various star formation rate (SFR) tracers. To estimate  $\tau_{\text{depl}}$ , we use new NOEMA observations of the  $^{12}\text{CO}(1-0)$  emission tracing the bulk molecular gas reservoir in NGC 2276, and extinction-corrected  $\text{H}\alpha$  measurements obtained with the PMAS/PPaK integral field unit for robust estimates of the SFR. We find a systematic decrease in  $\tau_{\text{depl}}$  of 1–1.5 dex across the disk of NGC 2276, with a further, abrupt drop in  $\tau_{\text{depl}}$  of  $\sim 1$  dex along the galaxy's western edge. The global  $\tau_{\text{depl}}$  in NGC 2276 is  $\tau_{\text{depl}} = 0.55$  Gyr, consistent with literature measurements for the nearby galaxy population. Such a large range in  $\tau_{\text{depl}}$  on subkiloparsec scales has never previously been observed within an individual isolated or premerger system. When using a metallicity-dependent molecular gas conversion factor  $X_{\text{CO}}$  the variation decreases by 0.5 dex. We attribute the variation in  $\tau_{\text{depl}}$  to the influence of galactic-scale tidal forces and ram pressure on NGC 2276's molecular interstellar medium. Our observations add to the growing body of numerical and observational evidence that galaxy–galaxy interactions significantly modify the molecular gas properties and star-forming activity within galactic disks throughout the interaction, and not just during the final merger phase.

*Key words:* galaxies: individual (NGC 2276) – galaxies: ISM – galaxies: star formation

## 1. Introduction

Star formation (SF) is a key process in the evolution of galaxies, affecting both their stellar populations and the properties of their interstellar medium (ISM). The star formation rate (SFR) and the bulk molecular gas ( $\text{H}_2$ ) correlate well in nearby galaxies, both locally (e.g., Bigiel et al. 2008; Leroy et al. 2013) and globally (e.g., Kennicutt 1998). The ratio between the  $\text{H}_2$  mass and SFR yields the depletion time of the  $\text{H}_2$ , i.e., the time needed to deplete the molecular gas reservoir assuming that the current SFR is constant,  $\tau_{\text{depl}} = M_{\text{H}_2}/\text{SFR}$ . A characteristic  $\tau_{\text{depl}}$  of 1–2 Gyr is observed for local normal star-forming disk galaxies on the main sequence (Saintonge et al. 2011; Leroy et al. 2013). Surveys of nearby galaxies show a scatter in  $\tau_{\text{depl}}$  of  $\sim 0.3$  dex at galactic and subgalactic scales (Saintonge et al. 2011; Leroy et al. 2013). However, interacting starburst galaxies (Klaas et al. 2010; Nehlig et al. 2016; Saito et al. 2016) and ultra-luminous infrared galaxies (LIRGs, ULIRGs; Saintonge et al. 2011; Martinez-Badenes et al. 2012) exhibit a lower systematic  $\tau_{\text{depl}}$  of 0.05–0.8 Gyr.

Investigations into the physics that drive variations in  $\tau_{\text{depl}}$  among and within galaxies are still ongoing. Stellar feedback

and molecular cloud evolution have each been put forward to explain these variations, but there is increasing evidence that internal and external galactic dynamics also affect  $\tau_{\text{depl}}$ . An example of internal dynamical processes is gravitational torques caused by galactic stellar structures, observed to modify the  $\tau_{\text{depl}}$  in the spiral arms of M51 (Meidt et al. 2013). Observations and numerical work indicate that external dynamical processes such as gravitation can also produce compressive and disruptive tides within galaxy gas disks during galaxy–galaxy interactions, leading to a broader distribution of  $\tau_{\text{depl}}$  (Renaud et al. 2014; Bournaud et al. 2015). Ram pressure, as another external force, is known for quenching SF, particularly in dwarf galaxies (Steinhauser et al. 2016), but can also locally compress gas and have the opposite effect (Ebeling et al. 2014), especially in more massive systems where the background potential helps to slow down gas stripping. Studies of  $\tau_{\text{depl}}$  in galaxies at various stages of interaction indicate that the tidal gravitational forces change  $\tau_{\text{depl}}$  up to 0.4 dex (Martinez-Badenes et al. 2012; Nehlig et al. 2016; Lee et al. 2017). Nehlig et al. (2016) observed that ram pressure can decrease  $\tau_{\text{depl}}$ , but not as effectively as the tidal effects. Within starburst-like interacting galaxies,  $\tau_{\text{depl}}$  can vary by up to 1 dex (Pereira-Santaella et al. 2016; Saito et al. 2016). F. Renaud (2018, in preparation, private communication) also conclude from their simulations of interacting galaxies that tidal forces generally decrease  $\tau_{\text{depl}}$  and increase its variation within galaxies. The aforementioned studies only address moderate to late stages of galaxy interactions, where the



Original content from this work may be used under the terms of the [Creative Commons Attribution 3.0 licence](https://creativecommons.org/licenses/by/3.0/). Any further distribution of this work must maintain attribution to the author(s) and the title of the work, journal citation and DOI.

**Table 1**  
Global Properties of NGC 2276

Parameter	Value	Reference
R.A.	07 <sup>h</sup> 27 <sup>m</sup> 13 <sup>s</sup> .609	Peak in <sup>12</sup> CO( $J = 1 \rightarrow 0$ )
Decl.	85 <sup>d</sup> 45 <sup>m</sup> 16 <sup>s</sup> .361	Peak in <sup>12</sup> CO( $J = 1 \rightarrow 0$ )
Systematic velocity [km s <sup>-1</sup> ]	2416	Emission lines.
Distance [Mpc]	35.5 ± 2.5	NED <sup>a</sup> , Ackermann et al. (2012)
Scale [pc arcsec <sup>-1</sup> ]	170 ± 10	
Intergalactic medium density (IGM) [g cm <sup>-3</sup> ]	10 <sup>-27</sup>	Mulchaey et al. (1993), Rasmussen et al. (2006)
Projected distance from NGC 2300 [km s <sup>-1</sup> ]	75 ± 15	Rasmussen et al. (2006)
log $M_{\text{stellar}}[M_{\odot}]$ of NGC 2300	11.3	From $K$ -band, and from 3.4 and 4.6 $\mu\text{m}$ ( <i>WISE</i> ; using Querejeta et al. 2015)
Line-of-sight velocity relative to IGM [km s <sup>-1</sup> ]	≈300	Rasmussen et al. (2006)
Inclination	≈20° ± 10°	From radial velocities and radial stellar profile
$R_{25}$ [kpc]	67'' = 11.6	HyperLeda <sup>b</sup>
log $M_{\text{stellar}}[M_{\odot}]$	10.7 ± 0.2	From 3.4 $\mu\text{m}$ and 4.6 $\mu\text{m}$ ( <i>WISE</i> ; using Querejeta et al. 2015)
log $M_{\text{H}_2}[M_{\odot}]$	9.8 ± 0.05	From <sup>12</sup> CO( $J = 1 \rightarrow 0$ ) estimated in this paper
log $M_{\text{H}_1}[M_{\odot}]$	9.8	Rasmussen et al. (2006)
$M_{\text{H}_1}/M_{\text{stellar}}$	0.13	
log $L_{\text{IR}}[L_{\odot}]$	10.75 ± 0.05	From IRAS; Sanders et al. (2003)
SFR( $H\alpha$ , corr)[ $M_{\odot} \text{ yr}^{-1}$ ]	17 ± 5	From the integrated spectra
SFR( $FUV + 22 \mu\text{m}$ )[ $M_{\odot} \text{ yr}^{-1}$ ]	≈10	From FUV and 22 $\mu\text{m}$ maps
SFR[ $M_{\odot} \text{ yr}^{-1}$ ]	5–19	Literature (Kennicutt 1983; Wolter et al. 2015).

#### Notes.

<sup>a</sup> <https://ned.ipac.caltech.edu/>

<sup>b</sup> <http://leda.univ-lyon1.fr/>

galaxies are already colliding or interacting at small separation from each other.

Here we study the spiral galaxy NGC 2276, which is currently falling into the NGC 2300 group and interacting with the early-type galaxy NGC 2300. The NGC 2300 group has four members including NGC 2300, which is the most massive one. Details about NGC 2276 and the NGC 2300 group are listed in Table 1. NGC 2276 itself exhibits high global SFR and an asymmetric distribution in various multiwavelength SFR tracers (X-Ray, FUV,  $H\alpha$ , infrared, and radio; Condon 1983; Gruendl et al. 1993; Davis et al. 1997; Rasmussen et al. 2006). These different tracers indicate SFRs between 5 and 19.4  $M_{\odot} \text{ yr}^{-1}$  (Kennicutt 1983; Wolter et al. 2015). Thus for its stellar mass, NGC 2276 is too star-forming to be on the main sequence (expected SFR ≈ 5–6  $M_{\odot} \text{ yr}^{-1}$ ; Elbaz et al. 2007). NGC 2276's total infrared emission is ≈ 5.6 × 10<sup>10</sup>  $L_{\odot}$ , which is not bright enough to be classified as an LIRG.

Previous papers (Gruendl et al. 1993; Hummel & Beck 1995; Rasmussen et al. 2006; Wolter et al. 2015) argue that the enhanced and asymmetric SF in NGC 2276 may be caused by tidal forces or ram pressure. While these papers argue that NGC 2276 is in a phase after the first passage through the pericenter, they do not derive specific orbital characteristics for this system. Tidal forces could be sufficient to trigger SF despite the large projected separation (≈75 kpc) to neighbor NGC 2300, as Scudder et al. (2012) show in their simulations that SFR may be enhanced by 0.3–0.6 dex at large separations (up to 70 kpc) between merging galaxies. The presence of tidal forces in NGC 2276 has also been invoked to explain the extended southeast arm in radio emission of NGC 2276 (Condon 1983), and truncation of the  $R$ -band continuum (Gruendl et al. 1993; Davis et al. 1997). Additional evidence for tidal forces includes a northeast extension in the  $I$ -band continuum of NGC 2300 (Forbes & Thomson 1992;

Davis et al. 1997), and the enhanced magnetic fields (Hummel & Beck 1995).

Enhanced X-ray emission outside NGC 2276, and the bow-shock feature on the western edge of NGC 2276's disk was attributed to ram pressure (Rasmussen et al. 2006) as similar features have been observed in galaxies with ongoing ram pressure (Iglesias-Paramo & Vilchez 1997; Sivanandam et al. 2014; Troncoso Iribarren et al. 2016). The high ram pressure acting on NGC 2276 is linked to the unusually high density of the group's intergalactic medium (Mulchaey et al. 1993). Simulations by Wolter et al. (2015) show that ram pressure alone could explain the morphology and the lack of some HI gas in NGC 2276.

Despite its exceptional SFR, the distribution of NGC 2276's molecular gas reservoir has not previously been mapped at high spatial resolution. Spatial variations in  $\tau_{\text{depl}}$  could indicate if tidal forces and/or ram pressure have an impact on the ISM physics and  $\tau_{\text{depl}}$  as such in NGC 2276. This Letter presents observations of  $\text{H}_2$  gas (as traced by CO emission) at subkiloparsec scales and spatially resolved measurements of  $\tau_{\text{depl}}$  in NGC 2276 for the first time. Additionally, we correct our integral field unit (IFU) measurements of  $H\alpha$  emission from the star-forming regions for internal extinction caused by dust, an important step that has not been applied to previous studies of SF in NGC 2276 using narrowband imaging.

## 2. Data

Observations with the IFU PMAS in PPak mode (Kelz et al. 2006) on the Calar Alto 3.5 m telescope are used to obtain spatially resolved  $H\alpha$  emission. We observed a mosaic of 6 pointings (≈75'' in diameter) with three dither positions, covering the entire galaxy. The raw data were calibrated using the P3D software package (Sandin et al. 2010) and established

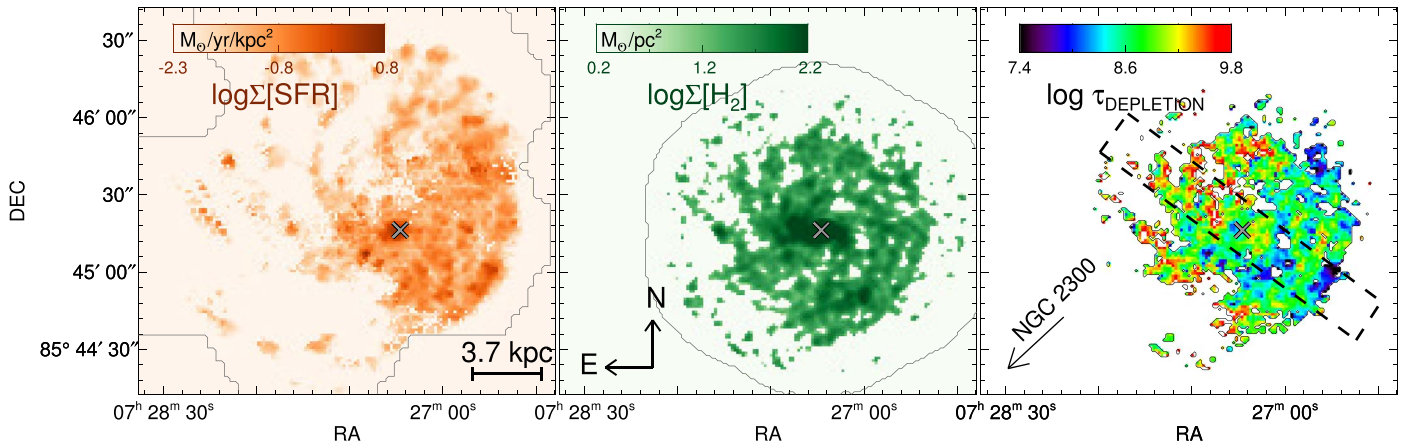


**Figure 1.** Distribution of  $\Sigma_{\text{SFR}}(\text{H}\alpha, \text{corr})$  (left),  $\Sigma_{\text{H}_2}$  (middle), and the depletion time  $\tau_{\text{depl}} (= \Sigma_{\text{H}_2} / \Sigma_{\text{SFR}}$ ; right) across the disk of NGC 2276. We indicate the areas observed in each tracer. In the panel showing the  $\tau_{\text{depl}}$ , we show the slit used to extract the data for the Kennicutt–Schmidt diagram in Figure 2 by a dashed rectangle. The slit orientation was chosen to encompass the largest range in  $\tau_{\text{depl}}$  values. Annotations indicate the direction toward the neighboring elliptical galaxy NGC 2300 and NGC 2276’s center (X symbol).

calibration procedures. We used PanSTARRS images for astrometry and *R*-band images from the La Palma observatory (NED<sup>9</sup>) for absolute flux calibration. The final datacube was resampled onto a grid with 1 arcsec spatial pixels (spaxels) corresponding to  $\approx 170$  pc. The datacube is Nyquist-sampled with  $\approx 3$  spaxels across the instrumental point-spread function. The reduced spectra have a spectral resolution of  $R = 1000$  and cover 3700–7010 Å. We analyzed the reduced spectra and extracted the emission lines using the GANDALF software package (Sarzi et al. 2006). During the process, the spectra were corrected for foreground Galactic extinction. The angular resolution of the final data is  $2''.7$  ( $\approx 450$  pc). More details will be provided in N. Tomičić (2018, in preparation).

To estimate the SFR surface density  $\Sigma_{\text{SFR}}(\text{H}\alpha, \text{corr})$ , we use extinction-corrected  $\text{H}\alpha$  surface brightness  $\Sigma(\text{H}\alpha, \text{corr})$ . Based on BPT diagrams (Kewley et al. 2006) of emission lines, we find that the  $\text{H}\alpha$  emission arises from star-forming regions and not from shocks. For the extinction correction, we assume the foreground screen model, apply the Cardelli et al. (1989) extinction curve, assume  $\text{H}\alpha/\text{H}\beta = 2.86$  (case B recombination at a gas temperature of  $\approx 10^4$  K) and a selective extinction  $R_V = 3.1$ . To convert  $\Sigma(\text{H}\alpha, \text{corr})$  to  $\Sigma_{\text{SFR}}(\text{H}\alpha, \text{corr})$ , we use the SFR prescription from Murphy et al. (2011, Equation (1) and (2)). We show the  $\Sigma_{\text{SFR}}(\text{H}\alpha, \text{corr})$  map of NGC 2276 in Figure 1.

To estimate the mass surface density of the  $\text{H}_2$  ( $\Sigma_{\text{H}_2}$ ), we mapped the  $^{12}\text{CO}(J = 1 \rightarrow 0)$  emission from NGC 2276 with the NOEMA interferometer at Plateau de Bure (NOEMA Extended Millimeter Array; project ID: w14cg001) and the IRAM 30 m telescope (project ID: 246-14). The NOEMA observations consisted of a 19-point hexagonal mosaic (with a field of view  $2'.2$  in diameter) centered on R.A. (J2000)  $07^{\text{h}}27^{\text{m}}14^{\text{s}}55$  and decl. (J2000)  $+85^{\text{d}}45^{\text{m}}16^{\text{s}}3$ . The 30 m observations covered a  $3 \times 3$  arcmin field centered on the same position. Both targeted the  $^{12}\text{CO}(J = 1 \rightarrow 0)$  emission assuming a systemic LSR velocity of  $2425 \text{ km s}^{-1}$ . The final combined (NOEMA+30m) cube has an angular resolution of  $2''.5 \times 2''.1$ , a channel width of  $5 \text{ km s}^{-1}$ , and  $1\sigma$  sensitivity of  $60 \text{ mK}$  per channel. For the analysis in this paper, we use a version of the cube that has been smoothed to  $2''.7$  resolution using a Gaussian convolution kernel. The sensitivity of this

cube is  $50 \text{ mK}$  per  $5 \text{ km s}^{-1}$  channel. More details will be presented in A. Hughes (2018, in preparation).

For  $\Sigma_{\text{H}_2}$ , we assumed the Galactic value  $X_{\text{CO}} = 2 \times 10^{20} \text{ cm}^{-2} (\text{K km s}^{-1})^{-1}$  (Bolatto et al. 2013) of the conversion factor. We show the  $\Sigma_{\text{H}_2}$  map of NGC 2276 in Figure 1. We use this conversion factor as NGC 2276’s nebular metallicity, estimated from the  $[\text{N II}]/[\text{S II}]$  and  $[\text{N II}]/\text{H}\alpha$  ratios and using Equation (3) in Dopita et al. (2016), is similar to the solar value ( $\log[\text{O}/\text{H}]+12$  ranges between 8.4 and 8.9). We also present in Figure 2 the NGC 2276 data for the case of a spatially varying  $X_{\text{CO}}$  factor taking into account local variation in metallicity.

### 3. Results

#### 3.1. The Depletion Time

The  $\Sigma(\text{H}_2)$  distribution is consistent with a fairly normal disk, while  $\Sigma_{\text{SFR}}(\text{H}\alpha, \text{corr})$  shows a prominent asymmetry toward the western edge (Figure 1). The resulting  $\tau_{\text{depl}}$  distribution is shown in Figure 1. The standard deviation of  $\tau_{\text{depl}}$  values is 0.52 dex. The highest observed  $\tau_{\text{depl}}(\text{H}_2)$  value is 9 Gyr, and it gradually decreases to 0.1 Gyr across the disk, from northeast (NE) to southwest (SW). The lowest  $\tau_{\text{depl}}$  values (10–100 Myr) are found along the western edge of the disk. The mean galactic  $\tau_{\text{depl}}$  value is 0.55 Gyr. From the integrated spectra, we estimate NGC 2276’s galactic SFR to be  $\approx 17 \pm 5 M_{\odot} \text{ yr}^{-1}$ .

To demonstrate the amplitude of the variation in  $\tau_{\text{depl}}$  in NGC 2276, we plot the pixel-by-pixel data on the Kennicutt–Schmidt diagram (Figure 2). The left panel shows NGC 2276 data from the  $20''$  wide slit oriented in the NE–SW direction (that follows the  $\tau_{\text{depl}}$  gradient), and other panels present NGC 2276 data from the entire disk. The right panel shows NGC 2276 data from the entire disk where we used a variable  $X_{\text{CO}}$  factor corrected for local variation in metallicity (Narayanan et al. 2012). The contours show the data from the HERACLES survey of nearby galaxies (Leroy et al. 2013), and the X symbol represents the NGC 2276’s mean galactic value. The HERACLES survey examines  $\sim 1$  kpc regions in 30 galaxies. We added subgalactic regions from the midstage merger VV 114 (Saito et al. 2015), luminous merger remnant NGC 1614 (Saito et al. 2016), and Antennae (Klaas et al. 2010). The NGC 2276 data from the slit show a decrease in  $\tau_{\text{depl}}$  from

<sup>9</sup> <https://ned.ipac.caltech.edu/>



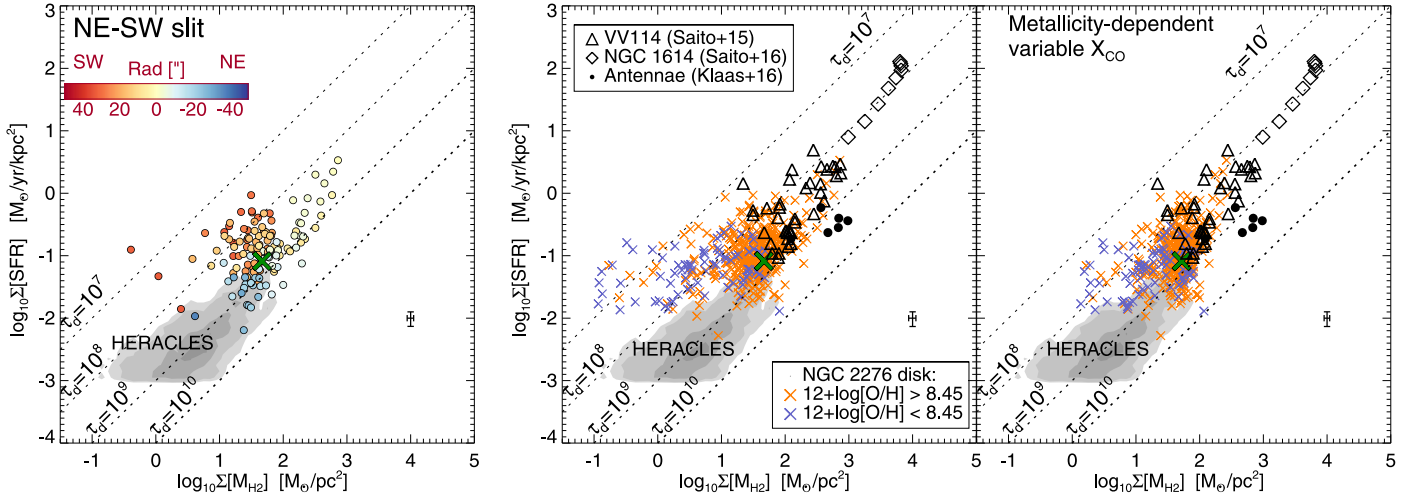


**Figure 2.** Large variation in the  $\tau_{\text{depl}}$  is seen across different regions of NGC 2276’s disk, and presented in the  $\Sigma_{\text{SFR}}(\text{H}\alpha, \text{corr})$  vs.  $\Sigma_{\text{H}_2}$  diagram (Kennicutt–Schmidt diagram). The left panel shows NGC 2276 data from the  $20''$  wide slit (shown in the right panel in Figure 1), which are color-coded from northeast (blue) to southwest (red). The middle and right panels present data from NGC 2276’s entire disk (blue and orange crosses for different metallicity ranges), the midstage merger VV 114 (Saito et al. 2015), the luminous merger remnant NGC 1614 (Saito et al. 2016), and the Antennae (Klaas et al. 2010). While we used constant  $X_{\text{CO}} = 2 \times 10^{20} \text{ cm}^{-2} (\text{K km s}^{-1})^{-1}$  for NGC 2276 data in the left and middle panels, on the right panel we applied an  $X_{\text{CO}}$  factor that takes into account the spatial variation in nebular metallicity (Narayanan et al. 2012). The contours present the data from the HERACLES survey of nearby galaxies at subgalactic scales (Leroy et al. 2013), and the green X symbol is the mean galactic value for NGC 2276 ( $\langle \tau_{\text{depl}} \rangle = 0.55$  Gyr). The pixels from the NGC 2276 maps are binned to sizes of  $2.''7$  ( $\approx 450$  pc) to show spatially independent data. Typical uncertainties are shown in the right corner. The dashed lines indicate  $\tau_{\text{depl}}$  of constant values.

3 Gyr to 10 Myr from NE toward SW, while the center exhibits a  $\tau_{\text{depl}}$  of about 0.4 Gyr. The  $\tau_{\text{depl}}$  values in the disk show a  $\approx 0.5$  dex narrower range when we use metallicity-dependent  $X_{\text{CO}}$  factor compared to when we use a single  $X_{\text{CO}}$  factor. The change in  $\tau_{\text{depl}}$  is most pronounced in the outskirts of the disk, especially the western edge, where metallicities are lower. However, we caution that metallicity estimates in the Western edge region could potentially be affected by the stellar cluster’s age, and thus ionization parameters (see Section 3.2).

### 3.2. Tidal Forces and Ram Pressure

Galactic-scale tidal forces are responsible for features such as stellar streams, disk thickening, and asymmetries in stellar disks. We derived  $\Sigma(M_{\text{stellar}})$  maps of NGC 2276 and NGC 2300 from *WISE* images at  $3.4 \mu\text{m}$  and  $4.6 \mu\text{m}$  following Equation (8) in Querejeta et al. (2015). The resulting map on Figure 3, confirms that the  $\Sigma(M_{\text{stellar}})$  distribution in NGC 2276 is strongly asymmetric, and shows a steeper drop on the SW side compared to the NE side. While other external (e.g., minor mergers, gas accretion) or internal (asymmetries in the dark matter halo) mechanisms cannot be ruled out as the origin of these features (Laine et al. 2014), we propose (as previous authors have done) that the asymmetric  $\Sigma(M_{\text{stellar}})$  in NGC 2276 is due to tidal forces.

To compare NGC 2276 to other galaxies, we quantify the tidal strength of the interaction  $Q$  experienced by NGC 2276 following Equation (1) in Argudo-Fernández et al. (2015), i.e.,

$$Q = \log_{10} \left[ \frac{M_{\text{comp}}}{M_{2276}} \left( \frac{D_{25}}{r} \right)^3 \right], \quad (1)$$

where  $\log(M_{\text{comp}}/M_{\odot}) = 10^{11.3}$  and  $\log(M_{2276}/M_{\odot}) = 10^{10.7}$  are the stellar masses of NGC 2300 and NGC 2276, respectively;  $D_{25}$  is the *B*-band optical diameter of NGC 2276, and  $r = 75$  kpc is the projected separation between NGC 2300 and NGC 2276. For NGC 2276, we find  $Q = -0.9$ , which is significantly higher than the typical value for isolated galaxies

( $Q = -5.2 \pm 0.8$ ) and on the high end of isolated galaxy pairs ( $Q = -2.3 \pm 1.2$ , Argudo-Fernández et al. 2015).

As well as galactic-scale tides, our new observations also show evidence for ram pressure affecting NGC 2276. First, the scale-length of the ionized gas on the SW side of NGC 2276’s disk is significantly shorter (up to 1–2 kpc) than the stellar emission scale-length (Figure 3). In contrast, the ionized gas follows well the stellar distribution on the NE side. This feature cannot be explained by tidal forces alone, and may be a signature of ram pressure stripping of the interstellar gas. Second, the  $\text{H}\alpha, \text{corr}/f_{\nu}$  ( $\text{FUV}, \text{corr}$ ) ratio increase along the western rim of NGC 2276’s disk (Figure 4). We retrieved the FUV images from the public AIS survey<sup>10</sup> (Bianchi et al. 2014). To calibrate the FUV images, we subtracted the background emission from NGC 2276, and corrected the FUV map for the foreground Milky Way extinction (applying  $E_{B-V} = 0.088$ ). The  $\text{H}\alpha, \text{corr}/f_{\nu}$  ( $\text{FUV}, \text{corr}$ ) ratio robustly indicates the age of stellar clusters (Sánchez-Gil et al. 2011), showing that the westernmost regions are dominated by the youngest clusters. We link this most recent SF on the western edge of the disk to ram pressure (as similarly observed in the Large Magellanic Cloud by Piatti et al. 2018).

## 4. Discussion and Summary

In this Letter, we have presented spatially resolved measurements of the  $\text{H}_2$  and  $\tau_{\text{depl}}$  in NGC 2276 for the first time. On galactic scales, the mean  $\tau_{\text{depl}}$  of NGC 2276 is 0.55 Gyr, which is lower than the  $\tau_{\text{depl}} = 1\text{--}2$  Gyr found in surveys of nearby galaxies (COLD GASS, HERACLES; Saintonge et al. 2011; Leroy et al. 2013), but still within the  $\tau_{\text{depl}}$  range of those galaxies (Figure 2 or Figure 14 in Leroy et al. 2013). We note that NGC 2276 exhibits  $\Sigma_{\text{SFR}}(\text{H}\alpha, \text{corr})$  and  $\Sigma_{\text{H}_2}$  values that are higher than in the HERACLES survey, and lower values than in the galaxies at the coalescence phase (Saito et al. 2015, 2016). On the other hand, we observe a large

<sup>10</sup> <http://galex.stsci.edu/GR6/?page=tilelist&survey=ais>

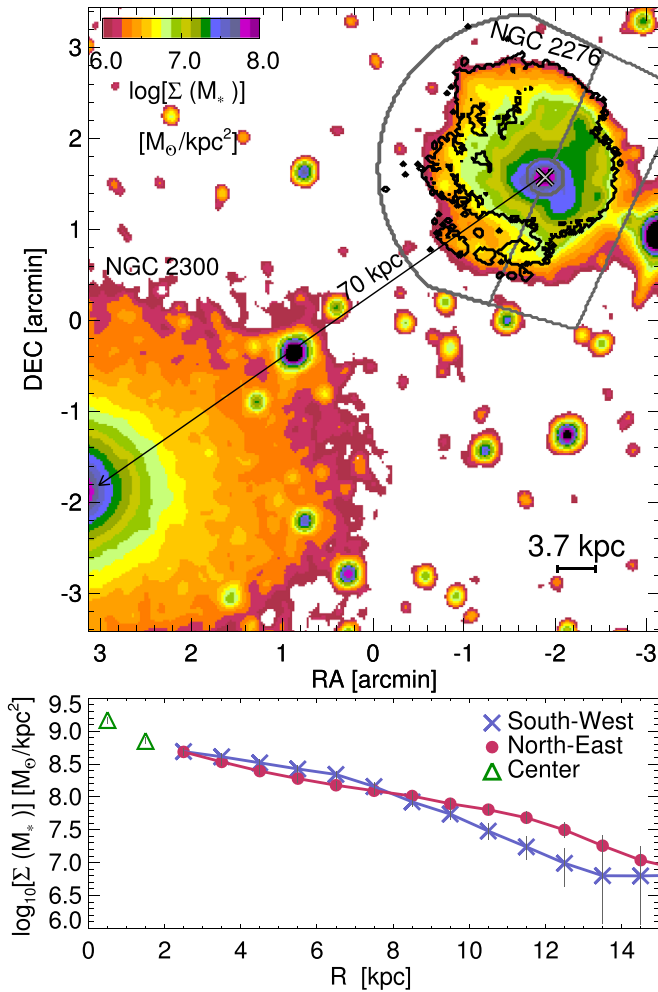


**Figure 3.**  $\Sigma(M_{\text{stellar}})$  of NGC 2276 and NGC 2300 derived from *WISE* images. NGC 2276’s stellar mass distribution is asymmetric and has a shorter scale-length on the southwest side compared to the northeast side. We attribute this to tidal forces exerted by NGC 2300. The black contour on NGC 2276 shows the observed  $H\alpha$  emission. The projected distance between the galaxies is marked. We show below a radial profile of  $\Sigma(M_{\text{stellar}})$  for the southwest (crosses), central (triangles), and northeast (circles) sides of NGC 2276 that are marked on the upper panel.

variation in  $\tau_{\text{depl}}$  at subgalactic scales in NGC 2276. On a pixel-to-pixel scale (pixels  $\approx 450$  pc in size) in a  $20''$  wide NE–SW slit,  $\tau_{\text{depl}}$  ranges from 10 Myr to 3 Gyr. This is almost 2–3 orders of magnitude variation in  $\tau_{\text{depl}}$  within a single disk. Furthermore, our results reveal a gradual decrease in  $\tau_{\text{depl}}$  across the disk in the NE–SW direction.

This is a factor of  $\approx 30$  larger range at subgalactic scales compared to other nearby galaxies. For individual galaxies in the HERACLES survey, subgalactic regions show a typical spread of  $\approx 0.5$  dex (Figure 18 and 19 in Leroy et al. 2013). However, a spread in NGC 2276’s  $\tau_{\text{depl}}$  decreases by 0.5 dex (down to 2.5 dex) when we use a variable metallicity-dependent  $X_{\text{CO}}$  factor, which indicates that subgalactic variation in  $\tau_{\text{depl}}$  may be affected by a different metallicity prescription or when using a single  $X_{\text{CO}}$  factor. The NGC 2276’s variation in the  $\tau_{\text{depl}}$  is comparable only with the merging starburst LIRGs observed by Pereira-Santaella et al. (2016) and Saito et al. (2016), though their mean galactic values exhibit lower  $\tau_{\text{depl}}$  than NGC 2276. The midstage merging galaxy VV114 (Saito et al. 2016) covers a similar

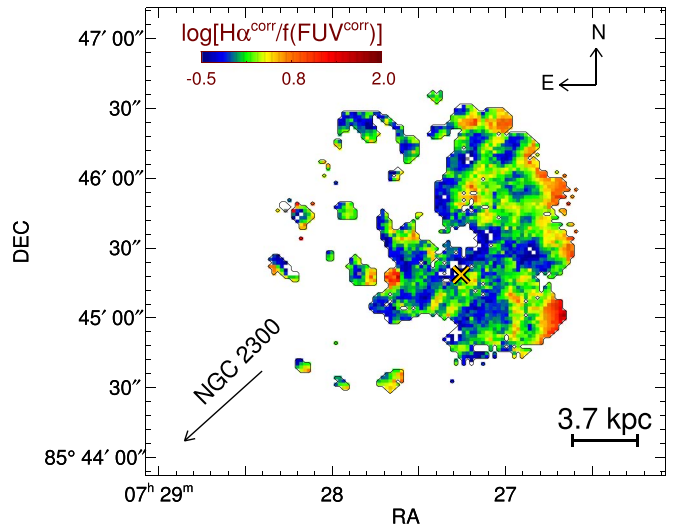


**Figure 4.**  $H\alpha, \text{corr}/f_\nu$  (FUV,corr) ratio map, with lower ratios robustly indicating older clusters (Sánchez-Gil et al. 2011). Shown data have  $S/N > 5$  in both Balmer lines and FUV emission. The mean uncertainty of the data shown is  $\approx 0.3$  dex. We attribute the increase in the ratio on the western edge of the disk to ram pressure triggering recent star formation.

range in parameters ( $\Sigma_{\text{SFR}}(H\alpha, \text{corr})$  and  $\Sigma_{\text{H}_2}$ ) as NGC 2276 on the Kennicutt–Schmidt diagram and shows almost 2 dex variation in  $\tau_{\text{depl}}$ . F. Renaud (2018, in preparation) find a 1–3 dex difference in  $\tau_{\text{depl}}$  between regions in their simulations of the Antennae during early phases of interaction. However, the observed variation in  $\tau_{\text{depl}}$  is only 0.5 dex in late-phase merging LIRGs such as the Antennae (Klaas et al. 2010) and NGC 4567/8 (Nehlig et al. 2016).

Based on the clear asymmetric distribution of the stellar disk, we tentatively attribute the large-scale gradient in  $\tau_{\text{depl}}$  as to tidal forces acting on NGC 2276. The tidal forces act on the entire disk, and likely cause a gradual 1–1.5 dex decrease of  $\tau_{\text{depl}}$  between the two sides of the disk. The ram pressure further disturbs the morphology of the gas disk, and particularly compresses gas on its western edge, which has younger stellar clusters and 1 dex lower  $\tau_{\text{depl}}$  compared to the rest of the disk.

NGC 2276 shows that galaxies in the pre-coalescence phase of interaction may already exhibit large variations in  $\tau_{\text{depl}}$  at subgalactic scales, while still showing a typical  $\tau_{\text{depl}}$  value for the galaxy-wide average. Our observations demonstrate clearly that a galaxy–galaxy interaction significantly modifies the SF efficiency of molecular gas locally, that the effect is distributed throughout the galactic disk and not just at the galaxy center, and that these changes occur well before coalescence.







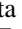
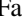

We thank the referee for constructive comments that improved this Letter. We thank Mónica Relaño, Rebecca McElroy, and Sharon Meidt for constructive comments on the paper. N.T. and K.K. acknowledge grants SCHI 536/8-2 and KR 4598/1-2 from the DFG Priority Program 1573. F.R. acknowledges support from the Knut and Alice Wallenberg Foundation. J.P. acknowledges support from the Program National “Physique et Chimie du Milieu Interstellaire” (PCMI) of CNRS/INSU with INC/INP, co-funded by CEA and CNES. This work is based on observations made with the NASA *Galaxy Evolution Explorer* (GALEX). GALEX is operated for NASA by the California Institute of Technology under NASA contract NAS5-98034. This work is based on observations

carried out under project number w14cg001 with the IRAM NOEMA Interferometer and 30 m telescope. IRAM is supported by INSU/CNRS (France), MPG (Germany), and IGN (Spain). This work is also based on observations collected at the Centro Astronómico Hispano-Alemán (CAHA), operated jointly by the Max-Planck Institut für Astronomie and the Instituto de Astrofísica de Andalucía (CSIC).

*Facilities:* IRAM (NOEMA and 30m), CSIC 3.5m (PMAS).

*Software:* P3D (Sandin et al. 2010), GANDALF (Sarzi et al. 2006).

### ORCID iDs

Neven Tomičić  <https://orcid.org/0000-0002-8238-9210>  
 Annie Hughes  <https://orcid.org/0000-0002-9181-1161>  
 Kathryn Kreckel  <https://orcid.org/0000-0001-6551-3091>  
 Florent Renaud  <https://orcid.org/0000-0001-5073-2267>  
 Jérôme Pety  <https://orcid.org/0000-0003-3061-6546>  
 Eva Schinnerer  <https://orcid.org/0000-0002-3933-7677>  
 Toshiaki Saito  <https://orcid.org/0000-0002-2501-9328>  
 Miguel Querejeta  <https://orcid.org/0000-0002-0472-1011>  
 Christopher M. Faesi  <https://orcid.org/0000-0001-5310-467X>  
 Santiago Garcia-Burillo  <https://orcid.org/0000-0003-0444-6897>

### References

- Ackermann, M., Ajello, M., Allafort, A., et al. 2012, *ApJ*, 755, 164  
 Argudo-Fernández, M., Verley, S., Bergond, G., et al. 2015, *A&A*, 578, A110  
 Bianchi, L., Conti, A., & Shiao, B. 2014, *AdSpR*, 53, 900  
 Bigiel, F., Leroy, A., Walter, F., et al. 2008, *AJ*, 136, 2846  
 Bolatto, A. D., Wolfire, M., & Leroy, A. K. 2013, *ARA&A*, 51, 207  
 Bournaud, F., Daddi, E., Weiß, A., et al. 2015, *A&A*, 575, A56  
 Cardelli, J. A., Clayton, G. C., & Mathis, J. S. 1989, *ApJ*, 345, 245  
 Condon, J. J. 1983, *ApJS*, 53, 459  
 Davis, D. S., Keel, W. C., Mulchaey, J. S., & Henning, P. A. 1997, *AJ*, 114, 613  
 Dopita, M. A., Kewley, L. J., Sutherland, R. S., & Nicholls, D. C. 2016, *Ap&SS*, 361, 61  
 Ebeling, H., Stephenson, L. N., & Edge, A. C. 2014, *ApJL*, 781, L40  
 Elbaz, D., Daddi, E., Le Borgne, D., et al. 2007, *A&A*, 468, 33  
 Forbes, D. A., & Thomson, R. C. 1992, *MNRAS*, 254, 723  
 Gruendl, R. A., Vogel, S. N., Davis, D. S., & Mulchaey, J. S. 1993, *ApJL*, 413, L81  
 Hummel, E., & Beck, R. 1995, *A&A*, 303, 691  
 Iglesias-Paramo, J., & Vilchez, J. M. 1997, *ApJ*, 479, 190  
 Kelz, A., Verheijen, M. A. W., Roth, M. M., et al. 2006, *PASP*, 118, 129  
 Kennicutt, R. C., Jr. 1983, *ApJ*, 272, 54  
 Kennicutt, R. C., Jr. 1998, *ApJ*, 498, 541  
 Kewley, L. J., Groves, B., Kauffmann, G., & Heckman, T. 2006, *MNRAS*, 372, 961  
 Klaas, U., Nielbock, M., Haas, M., Krause, O., & Schreiber, J. 2010, *A&A*, 518, L44  
 Laine, S., Knapen, J. H., Muñoz-Mateos, J.-C., et al. 2014, *MNRAS*, 444, 3015  
 Lee, B., Chung, A., Tonnesen, S., et al. 2017, *MNRAS*, 466, 1382  
 Leroy, A. K., Walter, F., Sandstrom, K., et al. 2013, *AJ*, 146, 19  
 Martínez-Badenes, V., Lisenfeld, U., Espada, D., et al. 2012, *A&A*, 540, A96  
 Meidt, S. E., Schinnerer, E., García-Burillo, S., et al. 2013, *ApJ*, 779, 45  
 Mulchaey, J. S., Davis, D. S., Mushotzky, R. F., & Burstein, D. 1993, *ApJL*, 404, L9  
 Murphy, E. J., Condon, J. J., Schinnerer, E., et al. 2011, *ApJ*, 737, 67  
 Narayanan, D., Krumholz, M. R., Ostriker, E. C., & Hernquist, L. 2012, *MNRAS*, 421, 3127  
 Nehlig, F., Vollmer, B., & Braine, J. 2016, *A&A*, 587, A108  
 Pereira-Santaella, M., Colina, L., García-Burillo, S., et al. 2016, *A&A*, 587, A44  
 Piatti, A. E., Cole, A. A., & Emptage, B. 2018, *MNRAS*, 473, 105  
 Querejeta, M., Meidt, S. E., Schinnerer, E., et al. 2015, *ApJS*, 219, 5  
 Rasmussen, J., Ponman, T. J., & Mulchaey, J. S. 2006, *MNRAS*, 370, 453  
 Renaud, F., Bournaud, F., Kraljic, K., & Duc, P.-A. 2014, *MNRAS*, 442, L33  
 Saintonge, A., Kauffmann, G., Wang, J., et al. 2011, *MNRAS*, 415, 61  
 Saito, T., Iono, D., Xu, C. K., et al. 2016, *PASJ*, 68, 20  
 Saito, T., Iono, D., Yun, M. S., et al. 2015, *ApJ*, 803, 60  
 Sánchez-Gil, M. C., Jones, D. H., Pérez, E., et al. 2011, *MNRAS*, 415, 753  
 Sanders, D. B., Mazzarella, J. M., Kim, D.-C., Surace, J. A., & Soifer, B. T. 2003, *AJ*, 126, 1607  
 Sandin, C., Becker, T., Roth, M. M., et al. 2010, *A&A*, 515, A35  
 Sarzi, M., Falcón-Barroso, J., Davies, R. L., et al. 2006, *MNRAS*, 366, 1151  
 Scudder, J. M., Ellison, S. L., Torrey, P., Patton, D. R., & Mendel, J. T. 2012, *MNRAS*, 426, 549  
 Sivanandam, S., Rieke, M. J., & Rieke, G. H. 2014, *ApJ*, 796, 89  
 Steinhauser, D., Schindler, S., & Springel, V. 2016, *A&A*, 591, A51  
 Troncoso Iribarren, P., Padilla, N., Contreras, S., et al. 2016, *Galax*, 4, 77  
 Wolter, A., Esposito, P., Mapelli, M., Pizzolato, F., & Ripamonti, E. 2015, *MNRAS*, 448, 781